Low temperature PECVD processes for the fabrication of integrated symmetrical resonant UV210 Organic/Semiconductor structures

Jordan Gastebois, Nathalie Coulon, Hervé Cormerais, Christophe Levallois, Eric Bêche, Jerome Esvan, Alain Moréac, Hervé Lhermite, Lucas Garnier, Bruno Bêche

Low temperature PECVD processes for the fabrication of integrated symmetrical resonant UV210 Organic/Semiconductor structures

J. Gastebois[a], N. Coulon[a], H. Cormerais[a, b], C. Levallois[c], E. Bêche[d], J. Esvan[e], A. Moréac[f,g], H. Lhermite[a], L. Garnier[a] and B. Bêche[a]

[a] *Univ Rennes, CNRS, IETR (Institut d'Electronique et des Technologies du numéRiques) - UMR 6164, F-35000 Rennes, France*
[b] *Centrale/Supelec, Campus de Rennes, F-35510 Cesson-Sévigné, France*
[c] *Univ Rennes, INSA Rennes, CNRS, FOTON (Fonction Optique pour les Technologies de l'informatiON) – UMR 6082, F-35000 Rennes, France*
[d] *Laboratoire PROMES – CNRS, 7 rue du four solaire, 66120, Font-Romeu Odeillo, France*
[e] *CIRIMAT, Université de Toulouse, CNRS, INP-ENSIACET, 4 allée Emile Monso, CS 44362, 31030 Toulouse cedex 4, France*
[f] *Univ Rennes, CNRS, IPR (Institut de Physique de Rennes) – UMR 6251, F-35000 Rennes, France*
[g] *Univ Rennes, UAR 2025 ScanMAT, F-35000, Rennes, France*

Email: jordan.gastebois@univ-rennes.fr ; bruno.beche@univ-rennes.fr

Keywords: Integrated organic photonic with PECVD; Semiconductor-On-Insulator with organic (SOI on Org.); Ellipsometric analyses; Raman analyses; XPS analyses; Resonators cavities.

Abstract

The resonant structures used as sensors for investigating specific dark and opaque substances may pose difficulties due to their potential aggressiveness towards photonic chips and the risk of destruction upon contact. To avoid it, this study presents a detailed description of a novel symmetrical waveguide structure with UV210 enclosed between Si/SiO_2 bi-layers implemented for integrated photonics. The fabrication process is thoroughly explained, accompanied by various analyses conducted for characterizations purposes. The structure is composed of an organic UV210 material developed using deep UV lithography at 248 nm and fabricated onto an oxidized silicon layer, resulting in a Si/SiO_2 bi-layer configuration. This process enables the fabrication of µm-scale access waveguides and racetrack Micro-Resonators (MRs) with a 400-nanometers gap. Several multilayer families have been produced using various low-temperature PECVD processes to obtain symmetrical Si/SiO_2/UV210/Si/SiO_2 structures and then properly characterized using non-destructive analyses and imaging techniques. The advantage of structural symmetry is primarily related to the electromagnetism and guidance equations, which eliminate the requirement for a cut-off thickness (or frequency), enabling significant miniaturization. Additionally, the upper cladding composed of a Si/SiO_2 bi-layer offers protection against potentially aggressive substances directly in contact with the organic waveguide core and MRs. Different bi-layer upper cladding families, produced under various PECVD conditions, were characterized using XPS to understand the bonding mechanism between the silicon and UV210 organic. In addition, ellipsometric analyses were conducted to determine the real and imaginary components of the refractive index of the global structure and the upper cladding bi-layer. Structure imaging were obtained by Raman analyses and optical statistical measurements were conducted on four different types of heterostructures, with silica temperatures ranging from 120°C to 150°C during the second PECVD process. The resonance analysis, performed through Free Spectral Range (FSR) measurements, allowed us to draw conclusions regarding the stability and reproducibility of the fabrication process, as well as the impact of PECVD processes conditions on the optical measurements. Such optoelectronic resonant elements and hybrid heterostructures enable the investigation of aggressive substances in direct contact.

1. Introduction

In the past few decades, integrated photonic and resonators have received considerable attention as a means to develop optical circuits for engineering [1], telecommunication [2–5] and sensing application [6,7]. Within optical cavities, a portion of the light, known as the evanescent field, extends beyond the core of the structure, enabling interactions with the surrounding environment [8,9]. This property has been used for various purposes, including label-free detection [10–13] and the investigation of soft matter behaviors directly in contact with the resonators [14,15]. Among the various materials explored for these applications, polymer waveguides fabricated using optical lithography have emerged as a central point of research [16]. This significance is attributed to their potential for integration onto microchips, biocompatibility [17], cost-effective production, and straightforward manipulation and relatively simple fabrication processes [18–22]. Recently, polymer micro resonators (MRs) manufactured through deep-UV lithography (DUV) technology allowing the development of sub-wavelength patterns have been used for the study of nano-particles (NPs) sedimentation in both water [23] and water-glycerol mixtures [24]. These resonant devices enable real-time analysis of colloidal systems in diverse solutions, including dark or opaque substances, with applications in energy, biology, and agriculture fields. Their studies provide insights into the dynamics of acid stratification in lead-acid batteries [25] and the performance of emerging colloidal electrolyte-based energy storage [26]. Within the petroleum industry, the investigation of colloidal stability during thermal reactions prevents the formation of obstructive coke [27]. Resonant structures applied to the dairy product industry can also be used to the detection of milk adulterants [28] and the study of dairy powder behavior during drying and evaporation [29]. However, a notable challenge associated with employing these resonant structures for sensing applications may be the potential damage when exposed to specific aggressive substances. The direct contact with such elements can compromise the overall integrity of the resonant elements, thereby limiting their durability and long-term functionality. To resolve this issue, the current paper presents a comprehensive approach to the development of a protective bi-layer Si/SiO_2 upper cladding located above the organic resonant element by associating Plasma Enhanced Chemical Vapor Deposition (PECVD) processes with DUV lithography processes. The complete fabrication processes and characterizations of an integrated photonic device are detailed by combining DUV lithography onto UV210 polymer associated with specific and adequate PECVD deposition processes at low temperatures. To obtain these hybrid heterostructures of organic UV210 sandwiched between thin layers of silicon and silicon oxides SiO_y, a low-temperature PECVD process was developed without oxygen gas at the initial growth stages and introduced later in a controlled manner. This strategy ensured the proper growth of protective SOI (Semiconductor-On-Insulator) layers over the organic guides and resonators, thereby preventing damage to the organic core from the highly reactive oxygen during PECVD. Consequently, these $Si/SiO_2/UV210/Si/SiO_2$ heterostructures exhibit a symmetrical material composition, featuring an oxidized Si wafer and a protective top layer of Si with growing silicon oxides.

In terms of electromagnetism, the calculation of propagation equations modes can be mathematically written as an eigenvalue and eigenvector problem [30,31]. Within integrated photonics using broadband light source, the eigenvalue of the complete optical structure results then in the effective group index, denoted as n_{eff}^{g}, which is intricately tied to the effective propagation constant $\beta = k_0\, n_{eff}^{g}$, where k_0 represents the wavenumber in the vacuum. These eigenvalues are solutions to opto-geometric equations called eigenvalue equations. For asymmetrical waveguides, solving these eigenvalue equations yields a critical value known as the cut-off thickness (or cut-off frequency), imposing a minimum thickness required for the propagation of a guided mode. The distinct feature of a symmetric waveguide is the absence of the cut-off thickness that characterizes asymmetrical waveguides [32]. Consequently, there are no longer physical limitations on the propagation of modes within the waveguide, regardless of its thickness, making way to a strong possible miniaturization of the structure. An example of symmetrical waveguide

exists in the form of Silicon-On-Insulator (SOI) which have been studied and successfully developed recently [33–35]. This technology presents a strong light confinement due to the large refractive index difference between silica and silicon and a possible miniaturization due to the symmetrization of the structure rendering it advantageous for optoelectronic circuit. SOI structures have been investigated for optoelectronic devices in the field of telecommunication [36–39] and hold promise for sensing applications [40–42]. In such applications, the sensing structure placed between oxide silicon layers can be protected from potentially corrosive agents.

In this way, this paper aims to realize various families of hybrid, symmetrical, single mode structures based on Semiconductor-On-Insulator technology incorporating organic UV210 components enclosed between Si/SiO_2 bi-layers (referred to SOI on Org.). MRs are made from the organic polymer UV210 [43] and obtained by DUV lithography on an oxidized silicon substrate, enhancing resolution capabilities [44]. For the upper cladding bi-layer, two consecutives depositions are made by PECVD at low temperature with different parameters [45]. To protect the organic material from the etching effects of highly reactive oxygen, silicon deposition is initially carried out in the absence of oxygen. Oxygen is subsequently introduced into the process in a controlled manner to ensure the growth of silicon oxides (similar to silica) above the organic material with good mechanical strength. Results are various symmetrical hybrid structures made of $Si/SiO_2/UV210/Si_{PECVD}/SiO_{2,\,PECVD}$ layers. Section 2 provides a proper description of the overall fabrication processes employed for different photonic structures families. This includes a meticulous depiction of the resonant element's geometry plus a selection of its dimensional parameters. Processes associated to various hybrid families defined by their PECVD deposition parameters are also exposed in this section. Subsequently, Section 3 shows a thorough devices characterizations through series of non-destructive analyses. The chemical signature of the deposited element and developed heterostructures imaging are obtained by Raman analyses in section 3.1. Following this, section 3.2 describes the interaction between silicon and organic resin UV210 after the first PECVD process via X-ray Photoelectron Spectroscopy. Section 3.3 undertakes a structure layer assessment at various fabrication stages. This evaluation is performed through ellipsometric spectroscopy, allowing the determination of opto-geometric parameters including layer thickness, refractive index, and absorption coefficient. Finally, all the various resonant structures are integrated into an experimental test platform in order to measure optical resonances upon excitation by a broadband source centered at a 795 nm wavelength. Different heterostructures resulting from distinct PECVD deposition conditions are studied in section IV and statistical measurements on Free Spectral Range (FSR) are discussed by indirectly providing information on composition by means of a pseudo-period measurement of the resonant signal and the corresponding effective group index. These heterostructures can subsequently be integrated into PECVD reactors to control material growth. Furthermore, a precise control over the stoichiometric composition of the upper cladding SiO_y, along with the bilayer thickness, allows for accurate adjustment of a precise FSR value for specific sensing applications.

2. Materials and processes for fabricating resonant symmetrical Organic/Semiconductor structures

2.1. UV210 organic resonant structure geometry, global circuit

Microstructures of resonant elements were fabricated through thin film deposition and photolithographic processes. The geometry and dimensions were meticulously determined using a software to design a quartz/chromium mask for photolithography. Fig. 1 illustrates the geometric element of the desired micro-resonators (MRs) coupled to the access waveguide. Multiple MRs enhances measurement precision by increasing resonant peak visibility and enables averaging, particularly beneficial for sensing applications. Furthermore, the shape of the designed racetrack increase the interaction with the access waveguide (increased L_c) to maximize coupling. The parameters of R, L_c and w are set at 5 µm for the radius of the MR, 5 µm for the coupling

length and 3 µm for the width of both the MR and the access waveguide. The gap is fixed at 400 nm for both physical and technical considerations. Furthermore, the tapered input of the access waveguide facilitated the injection during experimental tests.

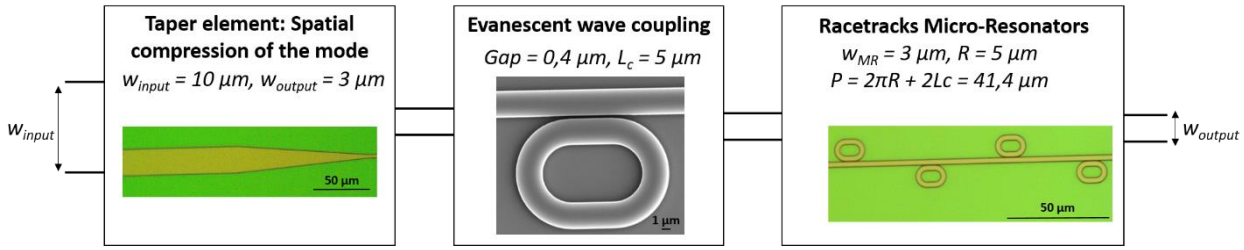

Fig. 1. Schematic representation of the architecture of the resonant circuits used as sensors. A racetrack-shaped micro-resonator is coupled to an access waveguide with an all-pass configuration. A taper structure is incorporated at the beginning of the latter to facilitate optical injection. The geometric parameters w_{input}, w_{output}, *gap*, L_c, w_{MR}, *R* and *P* represent the width of the waveguide at the input, the width of the waveguide at the output, the gap between the access waveguide and MRs, the interaction length coupling, the width of the MRs, the radius of the MRs and the perimeters of MRs, respectively. The three images made by optical microscope and scanning electron microscope (SEM) outline the three elements described in the circuit

Such structures have been made by photolithography in clean room environment [46]. Initially, a 1-2 µm thermal silica layer is grown on a silicon substrate by wet oxidation. The wafer undergoes a high-temperature treatment in a quartz oven during 4 hours at 1175°C followed by annealing between 700°C and 800°C to enhance the single crystal structure. The thickness of the silica layer facilitates mode propagation with minimal radiation loss and this lower cladding layer enhances the waveguide adhesion on the substrate. Subsequently, the resonant elements have been produced by photolithographic processes. Comprising a polymer that absorbs deep UV light, these elements enable photolithography at 248 nm, providing heightened precision compared to traditional photolithography at 365 nm. The UV210 polymer is an amplified chemical photoresist including a photo acid generator (PAG), enhancing sensitivity to UV energy exposure. This photoresist is spin coated onto the oxidized silicon wafer, achieving a typical height of 900 nm to ensure a light propagation into the photonic integrated circuits. Deep UV exposure is carried out using a mercury lamp (HBO 1000W/D, OSRAM) with an adequate filter and the previous quartz/chromium mask from TOPPAN PHOTOMASKS Inc. After a typical 30-seconds exposure, illuminated portion of the resin are removed to obtain the desired pattern using the tetramethyl ammonium hydroxide developer (Microposit MF CD-26). The molecular structure of the structure is stabilized with multiple softbake after all these steps. The use of the UV210 combined with lateral coupling allows the development of these resonant structures through a single illumination.

2.2. PECVD for various upper SOI bi-layer

The second delicate phase of the procedures is focused on creating the upper cladding bi-layer above the organic material to protect the resonant circuit and achieve symmetrical heterostructures with the organic layer sandwiched between Si/SiO2 layers. For this purpose, a two-step PECVD deposition at low temperature has been successfully developed with varying conditions. The initial PECVD deposition involves silane gas (SiH_4) at a substrate temperature of 120 or 150°C for 1 minute to create an amorphous silicon layer. This one is crucial to prevent a reaction between the organic material and the highly reactive oxygen present in the chambers that could damage the organic layer during the subsequent PECVD deposition. To achieve the desired SOI upper cladding, the second deposition was conducted using silane and a mixture of silane plus nitrous oxide (N_2O) as the gas reactor. Without the preceding silicon deposition, the organic might be susceptible to the etching effect of reactive oxygen. The amorphous silicon deposition resulting from the first PECVD process is conformal, meaning that silicon is deposited not only on the waveguide surface but also on its edges to provide protection when the silane is introduced subsequently. The second deposition was carried out at a substrate temperature ranging from 120 to 150°C with a duration varying from 1 to 6 minutes to obtain different layer

thicknesses which will be thoroughly characterized in the subsequent sections of the article. The overall treatment procedure is schematically illustrated in Fig. 2.

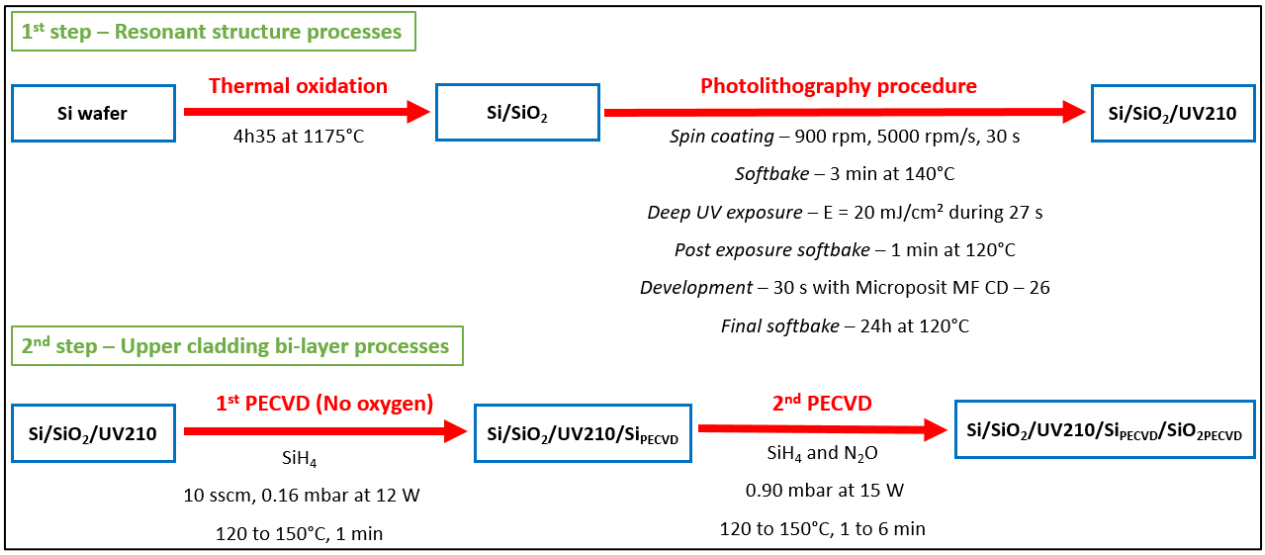

Fig. 2. Schematic representation of processes involved in the fabrication of symmetrical $Si/SiO_2/UV210/Si/SiO_2$ heterostructures.

In the following, heterostructures with various deposition conditions will be properly characterized through different analysis. A summary of the upper cladding deposition conditions, along with the next corresponding analyses, is presented in Tab. 1.

Analyses	Upper cladding deposition condition onto previous UV210 organic
Raman	Si, 120°C, 1 min SiO_2, 120°C, 1 min
XPS	Si, 120°C, 1 min
Ellipsometry	Si, 120°C, 1 min SiO_2, 135°C, 1 min
	Si, 120°C, 1 min SiO_2, 135°C, 3 min
	Si, 120°C, 1 min SiO_2, 135°C, 6 min

Tab. 1. Upper cladding deposition conditions by PECVD with the corresponding targeted analyses.

3. Structural characterizations of hybrid heterostructures

In the upcoming sections, a thorough examination of the heterostructures will be conducted. The initial two analysis, comprising Raman and XPS, reveal the physical-chemistry characteristics of those structures. Thereafter, the third analysis focuses on the optical property of the multi-layers through ellipsometric measurements.

3.1 Raman analyses

Raman analysis is a vibrational spectroscopic technique that provides insights into chemical composition. When photons interact with a sample, a small fraction undergoes a change in energy due to molecular vibrations. The scattered photons, known as Raman scattered light, carry information about these vibrational modes. Analysing the shifts in energy between the incident and scattered light reveals vibrational fingerprints, enabling the identification of molecular composition. The analysis, conducted on SOI/UV210/SOI structures, is performed using the LabRAM HR800 Raman Spectrometer (from Horiba Scientific Company, Jobin-Yvon). This spectrometer boasts high spectral resolution and is equipped with a confocal microscope, multiple laser sources (including 633 nm He-Ne, 785 nm Toptica, and 532 nm Coherent lasers), and nano-positioning capabilities. The integration with a

confocal microscope allows to perform two-dimensional imaging with a spatial resolution close to the spot size (0.9 µm²) at the focal plane, and a typical spectral resolution of 1 cm^{-1} per pixel. The laser excitation power used is lower than 0.1 mW to prevent any adverse heating effects on the photonics chip. Investigations utilized micro-Raman vibrational molecular spectroscopy to perform non-destructive material analysis. The results were recorded using the LabRAM HR 800 in the visible configuration. This approach enable to select specific areas within the structure for analysis, covering the entire wafer or specific cut sections, as depicted in Fig. 3. Micro-Raman spectroscopy was employed, allowing the detection and analysis of distinct signal signatures associated with various micro-materials, including Si and UV210. This facilitated the comprehensive examination of these specific components and their intricate signal characteristics.

The stretching mode of phenyl ring (s.m. CC) at 1002 cm^{-1} and the bending mode of aromatic olefinic (b.m. CCH) at 850 cm^{-1} are signature of the organic UV210 (Fig. 3)[47,48]. To isolate the organic UV210 peaks from the overall signal and eliminate any residual fluorescence background, filtering and decorrelation techniques were applied. Beyond the UV210 waveguide core, the Raman signal reveals the emergence of the first-order peak associated with crystalline silicon, attributed to the wafer and occurring at 521 cm^{-1} and the second order peak at 960 cm^{-1}. Just prior to this, there is a broader peak specific to the amorphous silicon, which is known to be deposited via PECVD. It is worth noting that the Raman signal specific to SiO_2 is exceptionally weak and remains practically invisible[49–52]. Furthermore, this signal extends toward lower frequencies in contrast to the more prominent signals of silicon and the organic UV210. By applying filtering techniques to refine the enlarged signature and selectively choosing the characteristic peaks of the various materials, such as Si and UV210, it becomes possible to perform two-dimensional imaging of the diverse waveguide/MR structures.

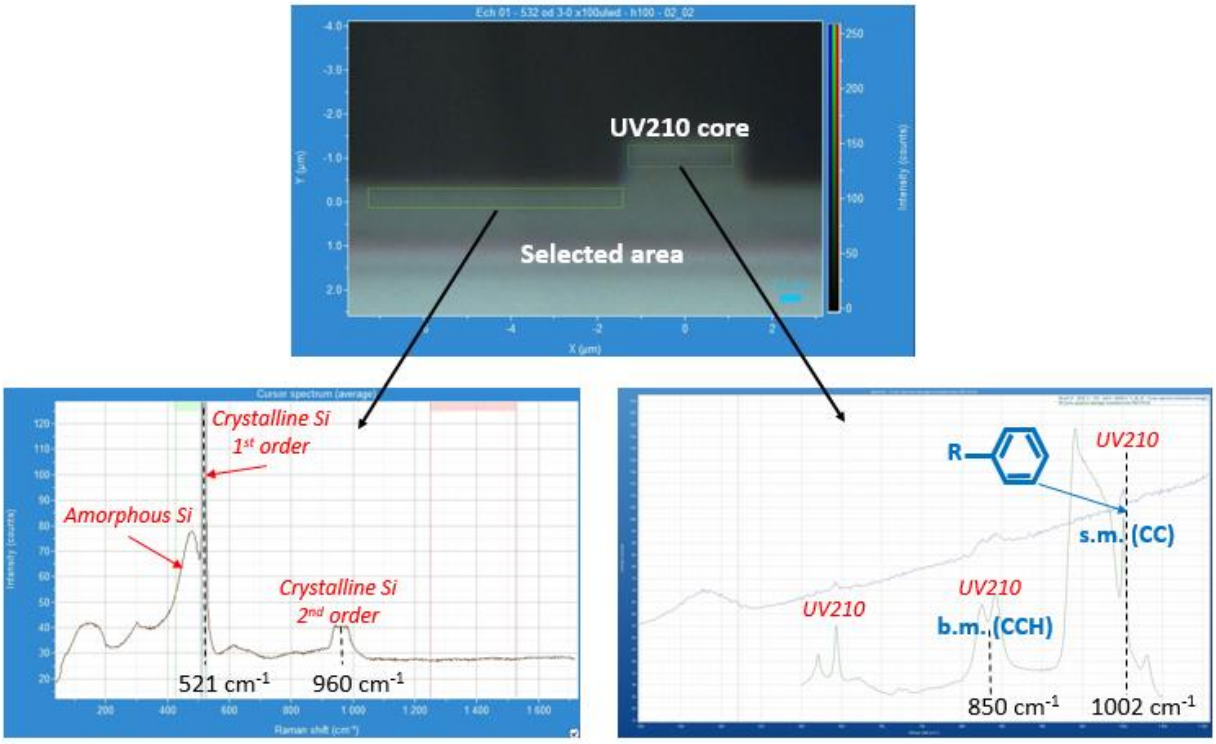

Fig. 3. Optical imaging of the waveguide cross-section plus Raman analyse of SOI with Org. structures performed on both the selected area (the UV210 rib waveguide and outside). The signature of the organic element as the deposited element by PECVD have been identified.

3.2 XPS analyses

In the following section, two distinct samples, Si/UV210 and Si/UV210/Si_{PECVD}, are subjected to X-ray Photoelectron Spectroscopy (XPS). This analysis is performed to compare chemical bonds and track the kinetic growth of the deposited element, with a focus on the interaction between the Silicon generated during the initial PECVD process and the organic UV210. When the material is irradiated with high-energy X-rays, XPS triggers the photoelectric effect, resulting in the emission of photoelectrons that bear distinct binding energies specific to their source atoms. This emission of photoelectrons provides crucial insights into the atomic composition and chemical environments within the material. Measurements were conducted using a KAlpha Thermoelectron device, and the photoelectron emission spectra were acquired with Al-Kα radiation ($h\nu$ = 1486.6 eV). An ion beam with an elliptical profile measuring 400 µm² was directed onto the samples. At each-second intervals, the corresponding binding energy peak analysis was performed. The binding energy scale was established by referencing the C 1s value of adventitious carbon (284.8 eV) [53]. The photoelectron peaks were analysed through Gaussian/Lorentzian (G/L=50) peak fitting, while the background signal was removed using the Shirley method [54].

XPS analyses were conducted on two distinct samples: one composed of organic UV210 and the other featuring an amorphous Si layer deposited onto the organic material by PECVD at low temperature (120°C). These analyses reveal energy peaks and the identification of chemical bonds at different phases of the deposition process, allowing for a comparison with a sample lacking a silica layer. Supplementary tables are available in the supplier information section for further reference. Fig. 4 illustrates the XPS composition profile obtained from the $Si_{substrate}$/UV210/Si_{PECVD} analysis, showing the atomic composition as a function of sputtering time. This figure clearly emphasize the material's growth throughout the processes and reveals three distinct zones: the surface, the interface, and the organic layers, corresponding to sputtering times of 0 seconds (surface), 170 to 210 seconds (interface UV210/Si_{PECVD}), and beyond 210 seconds (organic UV210). This temporal analysis provides valuable insights into the deposition process and material growth dynamics, offering a historical perspective on the changes in atomic composition over time. A summary of the quantitative atomic composition is provided in Tab. 2. In the following, the notation '1s' and '2p' represent the orbitals associated with quantum numbers (n=1, 2; ℓ=s, p). The numbers '1/2' and '3/2' indicate the spin-orbit splitting, denoting the intrinsic angular momentum of the electron (spin) and its interaction with its orbital angular momentum (ℓ) by $j = \ell \pm ½$.

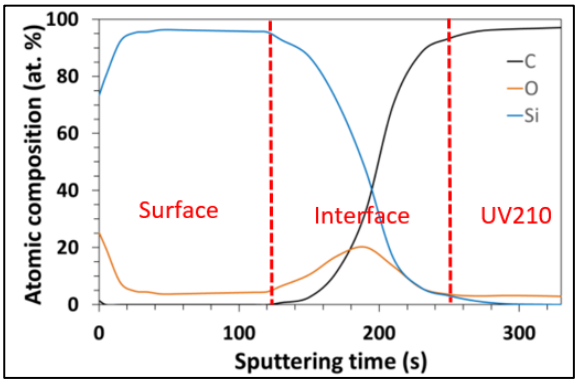

Fig. 4. Temporal evolution of the deposition process exhibits by the plot of the atomic composition (%) as a function of the sputtering

Sputtering time (s)	Atomic Compositions (%)		
	C	O	Si
0	1.4	25.2	73.4
45	0	3.7	96.3
170	11.8	17.1	71.1
210	70.1	13.5	16.4
310	96.9	3.1	Trace

Tab. 2. Atomic composition (%) measured from the C 1s, O, 1s and Si 2p core level spectra.

3.2.1 At the surface of the heterostructure: the amorphous silicon layer

Between 0 and 45 seconds of sputtering time, the surface of the sample is analysed. During this initial phase, a low concentration of atmospheric contaminants, specifically hydrocarbons, was detected and accounting for less than 2% of the composition. Additionally, a thin silicon oxide layer, approximately 20 Å thick, was observed due to natural oxidation. This oxide layer gradually decreased and is insignificant (< 4%) after 10 seconds of sputtering, marking the establishment of a new regime. At this point, the surface revealed the presence of a silicon layer resulting from the PECVD deposition process. At the 45-second mark, the Si 2p core level spectrum was deconvoluted into three distinct components, as illustrated in Fig. 5 and summarized in Tab. 3. The weakest Si 2p component, situated at 100.9 eV, is attributed to Si-O bonds, which are indicative of Si-O_x oxides contamination[55]. The other two components, at 99.0 eV and 99.6 eV, corresponding to Si $2p_{3/2}$ and Si $2p_{1/2}$ respectively, are associated with Si-Si_4 bonds, indicating pure silicon compounds where each silicon atom is surrounded by four neighbouring silicon atoms[56–58].

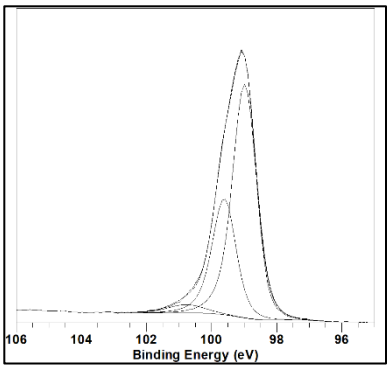

Fig. 5. Si $2p_{1/2,\ 3/2}$ spectrum collected for UV210/Si sample at 45 seconds of sputtering time.

Sputtering time (s)	Quantities measured	Components		
		$Si^0_{(3/2)}$	$Si^0_{(1/2)}$	$Si^{1+}_{(1/2,3/2)}$, $Si^{2+}_{(1/2,3/2)}$, $Si^{3+}_{(1/2,3/2)}$, $Si^{4+}_{(1/2,3/2)}$
45	Main component positions (eV)	99	99.6	100.9
	FWHM (eV)	0.9	0.9	1.1
	Percentage of each chemical bonds in the photoelectron peaks (%)	64.8	32.4	2.8
	Percentage of the chemical bonds related to the atomic compositions of each element (%)	62.4	31.2	2.7
	Nature of the chemical bonds	***Si - Si***	***Si - Si***	***SiO_x contamination***

Tab. 3. Main component positions (± 0.1 eV), FWHM (± 0.05 eV), percentage of each chemical bonds in the photoelectron peaks (Si $2p_{1/2,\ 3/2}$), and percentage of the chemical bonds related to the atomic compositions of each element (O, Si) for the UV210/Si sample at 45 seconds of sputtering time.

3.2.2 At the interface of the heterostructure: upper layer UV210/Si

The interface analysis takes place between 170 and 210 seconds of sputtering time, corresponding to the initial phase of the deposition process. Notably, there is a relatively high oxygen content (around 20%) at this interface due to residual oxygen present in the pump and chamber. The Si 2p core level spectrum is deconvoluted into six distinct components, as depicted in Fig. 6.a and summarized in Tab. 4. The two components associated with Si-Si_4 bonds, located at 99.0 and 99.6 eV, remain present. In contrast, the silicon oxide peaks are deconvoluted into four components positioned at 100.0, 101.1, 102.1, and 103.0 eV, indicative of Si-O bonds. This outcome reflects a mixture of "sub-oxides," denoted as Si_yO_x (Si-Si_yO_x with x + y = 4, comprising Si-Si_3O, Si-Si_2O_2, Si-

SiO_3, Si-O_4), with their relative proportions dependent on the concentrations of Si and O [55,59–65]. At 170 seconds of sputtering time, in close proximity to the Si layer, the main components are the Si $2p_{1/2}$ and Si $2p_{3/2}$ peaks (Fig. 6.a) whereas at 210 seconds of sputtering time, closer to the polymer, the Si 2p peaks are predominantly composed of "sub-oxides" (Fig. 6.b). This dynamic evolution over time highlights the varying composition of sub-oxides at the interface which is more significant at the beginning of the PECVD deposition.

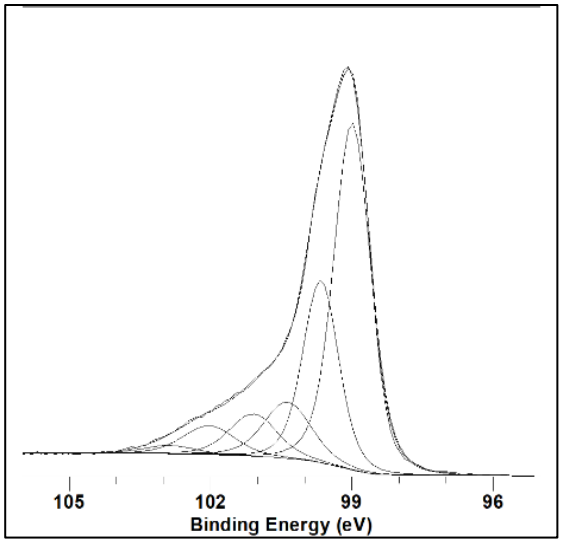

Fig. 6.a. Si $2p_{1/2,\ 3/2}$ spectrum collected for UV210/Si sample at 170 seconds of sputtering time.

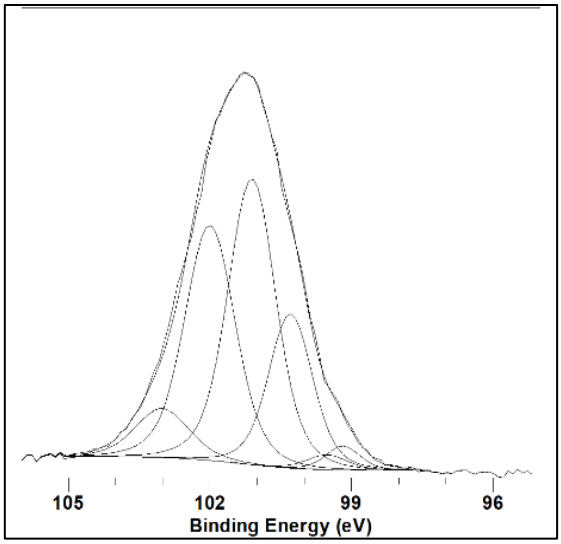

Fig. 6.b. Si $2p_{1/2,\ 3/2}$ spectrum collected for UV210/Si sample at 210 seconds of sputtering time.

Sputtering time (s)	Quantities measured	Components					
		$Si^0_{(3/2)}$	$Si^0_{(1/2)}$	$Si^{1+}_{(1/2,3/2)}$	$Si^{2+}_{(1/2,3/2)}$	$Si^{3+}_{(1/2,3/2)}$	$Si^{4+}_{(1/2,3/2)}$
170 s	Main component positions (eV)	99.0	99.6	100.2	101.1	102.1	103.0
	FWHM (eV)	0.9	0.9	1.0	1.1	1.2	1.3
	Percentage of each chemical bonds in the photoelectron peaks (%)	50	25.0	10.2	7.6	5.6	1.6
	Percentage of the chemical bonds related to the atomic compositions of each element (%)	35.6	17.8	7.25	5.4	4.0	1.1
	Nature of the chemical bonds	***Si – Si***	***Si – Si***	***Si – Si_3O***	***Si – Si_2O_2***	***Si – SiO_3***	***Si – O_4***
210 s	Main component positions (eV)	99.0	99.6	100.2	101.1	102.1	103.0
	FWHM (eV)	1.0	1.0	1.1	1.2	1.25	1.3
	Percentage of each chemical bonds in the photoelectron peaks (%)	2.2	1.1	18.7	38.3	32.5	7.2
	Percentage of the chemical bonds related to the atomic compositions of each element (%)	0.35	0.17	3.1	6.3	5.3	1.2
	Nature of the chemical bonds	***Si – Si***	***Si – Si***	***Si – Si_3O***	***Si – Si_2O_2***	***Si – SiO_3***	***Si – O_4***

Tab. 4. Main component positions (± 0.1 eV), FWHM (± 0.05 eV), percentage of each chemical bonds in the photoelectron peaks (Si $2p_{1/2,\ 3/2}$), and percentage of the chemical bonds related to the atomic compositions of each element (O, Si, C) for the UV210/Si sample at 170 and 210 seconds of sputtering time.

The C 1s core level spectrum is deconvoluted into four distinct components located at 282.8, 284.4, 285.8, and 288.8 eV (Fig. 7, Tab. 5). The predominant component is associated with the phenyl group, representing both Csp^2 and Csp^3 in C-C bonds, as well as the -CH3 methyl group, characteristic of the UV210 organic component[56,57,66,67].

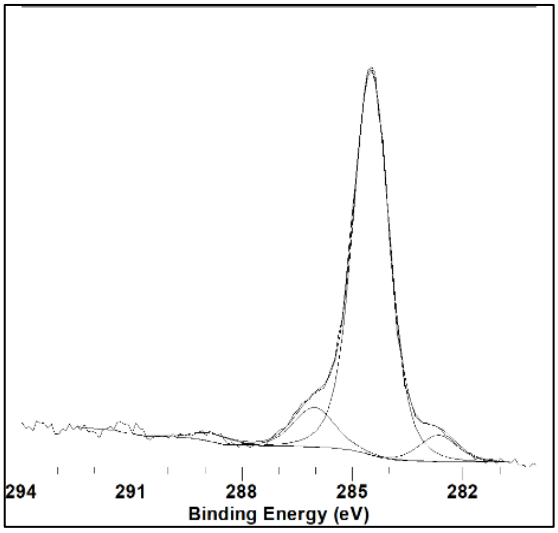

Fig. 7. C 1s spectrum collected for UV210/Si sample at 170 seconds of sputtering time.

Sputtering time (s)	Quantities measured	Components C 1s			
170 s	Main component positions (eV)	282.8	284.5	285.9	288.8
	FWHM (eV)	1.2	1.2	1.4	1.5
	Percentage of each chemical bonds in the photoelectron peaks (%)	5.4	82.4	10.1	2.2
	Percentage of the chemical bonds related to the atomic compositions of each element (%)	0.7	9.7	1.2	0.2
	Nature of the chemical bonds	***C – Si***	***C – C, C – H***	***C – O, C – OH***	***O = C – O***

Tab. 5. Main component positions (± 0.1 eV), FWHM (± 0.05 eV), percentage of each chemical bonds in the photoelectron peaks (C 1s), and percentage of the chemical bonds related to the atomic compositions of each element (O, Si, C) for the UV210/Si sample at 170 seconds of sputtering time.

3.2.3 At the core level: the UV210 organic

After 210 seconds of sputtering time, the study evaluates the composition of the UV210 organic. Ion sputtering affects the polymer by graphitizing the surface, promoting atomic recombination and the formation of new bonds. The analysis of the UV210/Si sample is compared to another sample composed of UV210 without any Si deposition (Fig. 8, 9, Tab. 6). The absence of C-Si bonds is noteworthy (% Si < 0.1), and the component at 284.5 eV, associated with carbon in the phenyl group, remains intact. The key distinction between the two samples lies in the reduced levels (for the UV210/Si sample) of C-O and C=O bonds due to bond breakage during treatment, along with the effects of ion sputtering. Additionally, the absence of the shake-up peak (π ->π* transitions) observed at 291.2 eV in the UV210/Si sample can be mainly attributed to the significant effect of the ionic sputtering process leading to the disruption of π-type bonds within the benzene rings of the UV210 polymer (graphitization and/or presence of induced carbon chemical environment [67,68]). The missing component in the UV210/Si sample at 287.1 eV and corresponding to O-C-O bonds may be due to the formation of new C-O type bonds as a result of polymerized chain reactions, the influence of the ion sputtering, and the recombination of C-O bonds leading to an increased O=C-O bonds[67,69–71].

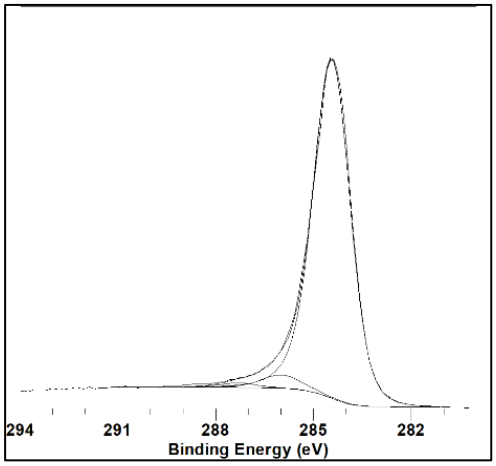

Fig. 8.a. C 1s spectrum collected for UV210/Si sample at 310 seconds of sputtering time.

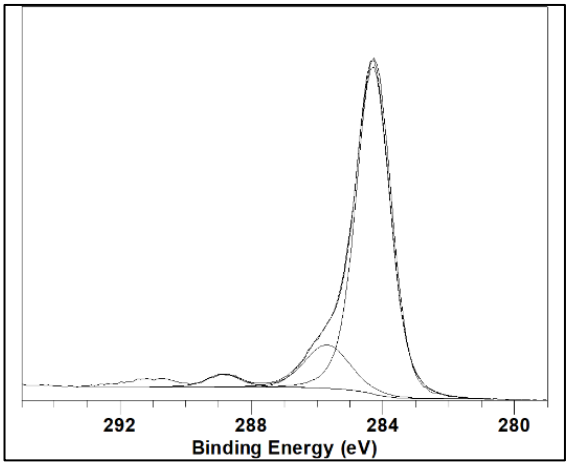

Fig. 8.b. C 1s spectrum collected for UV210 sample.

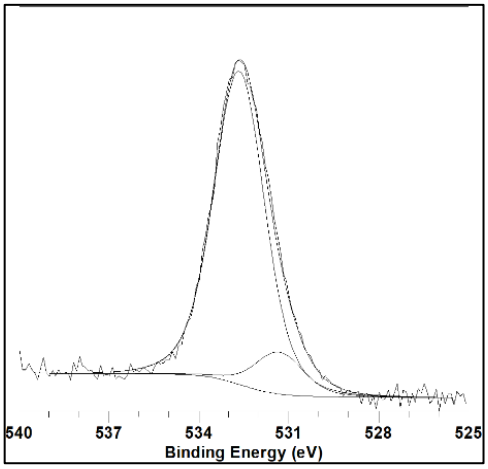

Fig. 9.a. O 1s spectrum collected for UV210/Si sample at 310 seconds of sputtering time.

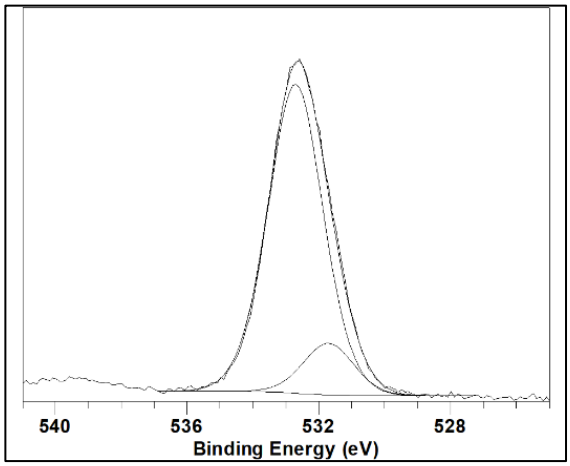

Fig. 9.b. O 1s spectrum collected for UV210 sample.

Sample	Quantities measured	Components						
		O 1s		C 1s				
UV210	Main component positions (eV)	531.7	532.9	284.4	285.8		288.5	291.4
	FWHM (eV)	1.7	1.8	1.2	1.4		1.5	1.7
	Percentage of each chemical bonds in the photoelectron peaks (%)	14.2	85.8	80.7	13.9		2.6	2.8
	Percentage of the chemical bonds related to the atomic compositions of each element (%)	1.8	10.8	70.5	12.15		2.3	2.45
	Nature of the chemical bonds	***O = C***	***O – C, O – H***	***C – C, C – H***	***C – O, C – OH***		***O = C – O***	***π→π* s.u***
UV210/Si	Main component positions (eV)	531.5	532.8	284.5	285.8	287.1	288.5	
	FWHM (eV)	1.8	1.9	1.2	1.4	1.4	1.5	
	Percentage of each chemical bonds in the photoelectron peaks (%)	10.3	89.7	96.2	3.0	0.6	0.2	
	Percentage of the chemical bonds related to the atomic compositions of each element (%)	0.3	2.8	93.2	0.9	0.6	0.2	
	Nature of the chemical bonds	***O = C***	***O – C***	***C – C, C – H***	***C – O, C – OH***	***O – C – O***	***O = C – O***	

Tab. 6. Main component positions (± 0.1 eV), FWHM (± 0.05 eV), percentage of each chemical bonds in the photoelectron peaks (O 1s, C 1s), and percentage of the chemical bonds related to the atomic compositions of each element (O, C) for the UV210/Si sample at 310 seconds of sputtering time and for the UV210 sample.

The XPS analysis provides valuable insights into the compositional changes and surface characteristics of the UV210/Si_{PECVD} system at different stages of sputtering time. The observed variations in chemical bonds and the presence of a mixture of "sub-oxides" at the interface provides information on the deposition conditions and demonstrate the non-destruction of the organic material by the initial PECVD deposition. It has shown the possibility to protect the organic and the MRs by an upper SOI bi-layer and to create symmetrical heterostructures Si/SiO_2/UV210/Si_{PECVD}/$SiO_{2,PECVD}$.

3.3 Ellipsometric analyses

The upper SOI bi-layer will be used as an upper cladding in integrated photonic so it is necessary to exanimate optical properties as the refractive index and absorption coefficient by ellipsometric measurement. It is a non-destructive surface measurement technique that enables access to the optical and physical properties of materials by analysing the polarization change of light following its reflection from a surface. This analysis yields the ellipsometric parameters, Δ and ψ, derived from the reflection coefficients, which are determined using the following relationships: $tan(\Psi) = \frac{|r_p|}{|r_s|}$ and $\Delta = \delta_p - \delta_s$, where r_p and r_s represent the polarizations parallel and perpendicular to the incidence plane, respectively. These reflection coefficients are expressed as $r_p = |r_p|exp(j\delta_p)$ *and* $r_s = |r_s|exp(j\delta_s)$. By plotting $I_s = \sin(2\psi)\sin(\Delta)$ and $I_c = \sin(2\psi)\cos(\Delta)$ as a function of wavelength (or photon energy), one can fit the data using a model with parameters[72,73]. The real (*n*) and imaginary (*k*) parts of the refractive index (*k* being linked to the absorption coefficient) can be deduced. Film thicknesses (*d*) can be also extracted from the fitting operation. Ellipsometric measurements were carried out on various heterostructures, as detailed in Tab. 7, to examine their intrinsic properties. These measurements are performed on both the upper cladding bi-layer and on the complete structure, enlighten on the thickness of the upper cladding resulting from PECVD processes at low temperatures. A Horiba Uvisel 2 ellipsometer (Fig. 10) was employed for these analyses, and the study spanned different stages of the symmetrical structure's fabrication process. The first analysis was conducted on a structure lacking the upper cladding, comprised of a Si/SiO_2/UV210 layer (Heterostructure type I). In the visible range (400 – 800 nm) where thermal SiO2 refractive indices are well known and k=0 can be assumed for the UV210 layer, a straightforward Cauchy model is completely suitable to deduce the real refractive index of the polymer layer (see Fig. 11). From this first fit a silica thickness of 1572 nm and a polymer thickness of 907 nm are deduced, consistent with previous studies. For the absorbent region (200 – 400 nm) where k≠0, a more advanced Tauc-Lorentz model usually used for amorphous material [74] was employed to fit the data. This model successfully captured the absorption peak at 280 nanometers, as depicted in Fig. 12, aligning with the data provided by the material supplier.

Fig. 10. Horiba Uvisel 2 spectrometer used for the ellipsometric measurements.

Heterostructures type	Upper cladding PECVD conditions
Type I	None
Type II	Si amorphous : 1 min at 120°C SiO_2 : 1 min at 135°C
Type III	Si amorphous : 1 min at 120°C SiO_2 : 3 min at 135°C
Type IV	Si amorphous : 1 min at 120°C SiO_2 : 6 min at 135°C

Tab. 7. PECVD conditions for the upper cladding bi-layer for four types of heterostructures.

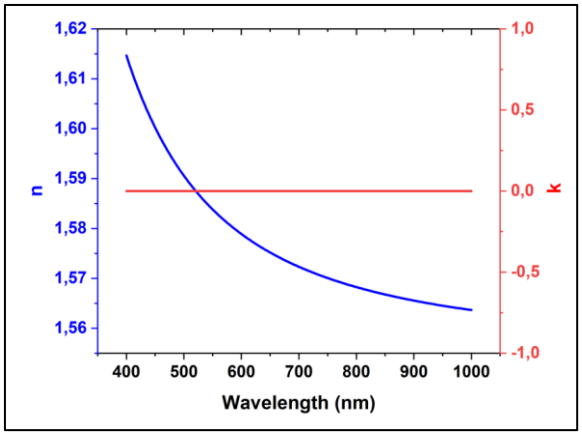

Fig. 11. Plot of *n* and *k* as a function of the wavelength for the transparent region using the Cauchy model for the Si/SiO_2/UV210 structure.

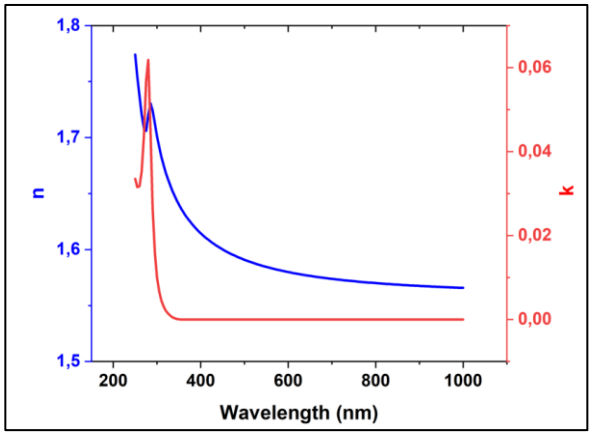

Fig. 12. Plot of *n* and *k* as a function of the wavelength for absorbent region using the double Tauc-Lorentz model for the Si/SiO_2/UV210 structure.

The different heterostructures upper cladding are then properly characterized (Heterostructures type II, III and IV). This bi-layer, comprising an amorphous silicon layer and a SiO_2 layer deposited via low-temperature PECVD, was also examined using an equivalent Tauc-Lorentz model. An excellent agreement between experimental data and fitting results was found. The plots of I_s and I_c as functions of wavelength for three angles used in VASE (Variable Angle Spectroscopic Ellipsometry) mode evidence this result (Fig. 13). This study enables the plot of the evolution of the refractive index (*n*) and absorption coefficient (*k*) as functions of wavelength for the three heterostructures (Fig. 14). The growth time of SiO_2 deposition resulted in an increase in the bi-layer's (amorphous silicon + SiO_2) thickness: 24.1 nm for 1 minute, 39.0 nm for 3 minutes, and 117 nm for 6 minutes. At 800 nm, a thicker bi-layer led to a lower *k*, indicating decreased absorption. According to the Kramer-Kronig relation, this also corresponded to a lower real part of the refractive index which is a Hilbert transformation property in mathematics. The observed decrease in absorption with increased thickness can be attributed to a composition gradient with inherent defects during the deposition process. As observed in the XPS analysis, the composition of sub-oxide SiO_y at the interface may vary with the PECVD deposition time, consequently influencing the parameters *n* and *k*. In other terms, changes in the stoichiometric ratio SiO_y result in variations in the intrinsic refractive index of the bi-layer.

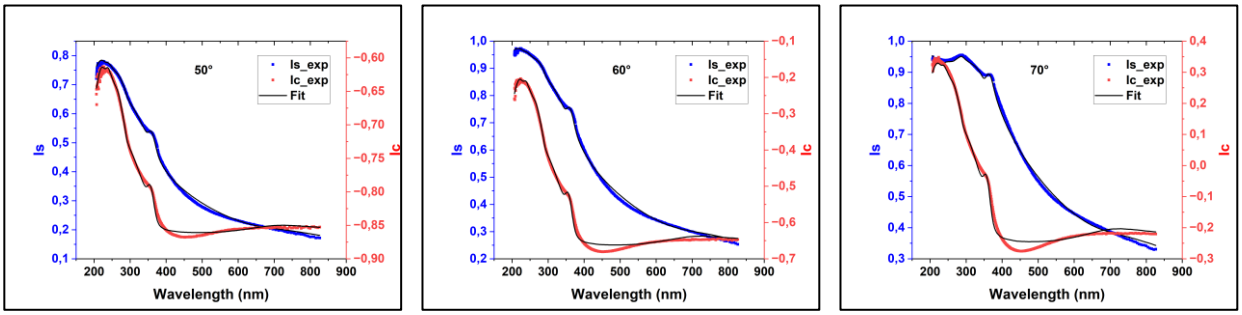

Fig. 13. The plot of I_s and I_c as a function of the wavelength for various angle using the VASE method shows a good agreement between the data and the Tauc-Lorentz model for the heterostructure type II.

The last ellipsometric analysis was conducted on the overall symmetrical structure Si/SiO_2/UV210/Si/SiO_2 by combining the model used for the Si/SiO_2/UV210 structure and the one for the upper cladding (with PECVD condition type II). The results once again demonstrate a strong agreement between the data and the fitted model (Fig. 15), indicating an amorphous silicon layer

thickness of 18.6 nm and a SiO_2 thickness of 28.9 nm. In the following section, these variations will be characterized by measuring the resonant signal (with its associated effective group index) in other heterostructures, differentiated by the temperature conditions during PECVD deposition.

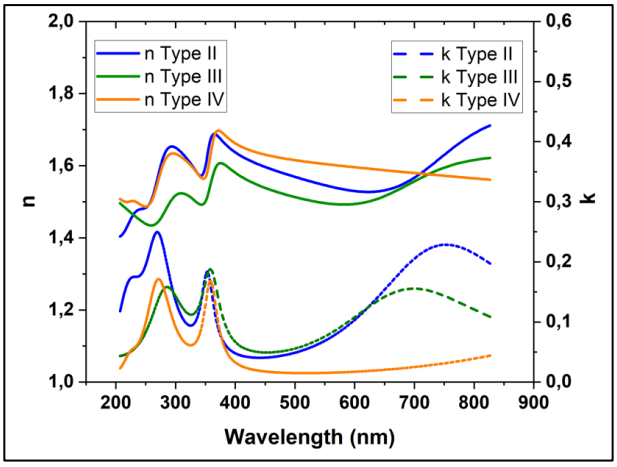

Fig. 14. Plot of *n* and *k* as a function of the wavelength for heterostructures types II (bi-layer thickness = 24.1 nm), III (bi-layer thickness = 39.0 nm) and IV (bi-layer thickness = 117 nm). A composition gradient can be seen as the absorption coefficient decrease as the SiO_2 thickness increase.

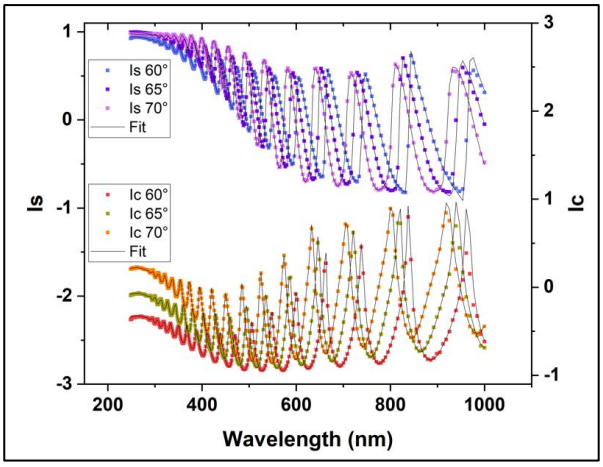

Fig. 15. The plot of I_s and I_c as a function of the wavelength for various angle using the VASE method shows a good agreement between the data and models used for the overall symmetrical structure.

Then, the optical indices of the $Si_{amorphous}/SiO_2$ bi-layer are suitable for serving as the upper cladding in guided optics. This implies the feasibility of developing a symmetrical heterostructure, SOI/UV210/SOI, by incorporating a UV210 organic layer sandwiched between two SOI layers.

4. Optical resonant measurements and discussion

4.1. Principle and optical experimental platform

Resonant structures are used for sensing applications, where the transduced resonant signal is measured by tracking the Free Spectral Range (FSR) evolution. The establishment of stationary waves within Micro-Resonators (MRs) is achieved through evanescent coupling between the access waveguide and MRs. The spectral difference between two consecutive resonant wavelengths is linked to the effective refractive index of the entire structure by the formula: $FSR = \frac{\lambda_0^2}{P.n_{eff}^{gpe}}$, where λ_0 is the central excitation wavelength and P is the MR perimeter. To perform FSR measurements, the photonic chip is integrated onto an optical test platform. The incident beam comes from a broadband laser diode source (SUPERLUM, SLD 331 HP3, λ_0 = 795 nm, and a 40 nm spectrum width) while the output is connected to a CCD camera for micro-injection control. Injection precision is monitored through nano-piezoelectric actuators (PI-5631.3 E), and the signal is analysed with a spectrometer (HR 4000, Ocean Optics). A Matlab interface enables the control of the analyser, data collection, and real-time Fast Fourier Transform on the spectrum to capture the dynamic evolution of the FSR. The schematic representation of all these elements is illustrated in Fig. 16. This experimental optical test platform ensures a statistical measurement of the FSR across different heterostructures.

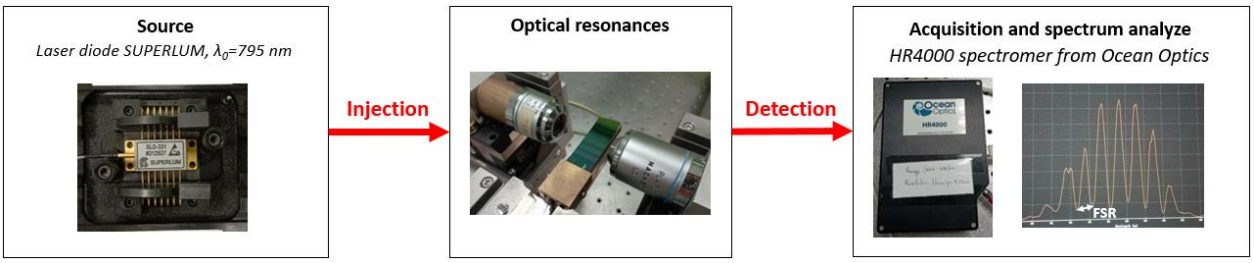

Fig. 16. Schematic representation of the optical test platform from the source (broadband laser diode SUPERLUM) to the spectrum analyse (with the HR4000 spectrometer linked to a computer and piloted through a real-time Matlab interface).

4.2. Effect of the SiO_2 temperature deposition on the resonances

Measurements were conducted on various symmetrical heterostructures to assess the stability of resonances and understand the impact of upper cladding deposition conditions on resonant measurements. To this end, statistical Free Spectral Range (FSR) measurements were performed on four heterostructures with different temperature depositions of the SiO_2 upper cladding (Tab. 8). Notably, the FSR measurements exhibited stability for any deposition conditions (Fig. 17), indicating a high level of knowledge and reproducibility in the deposition processes. Furthermore, the observed inverse relationship between the FSR and the temperature of SiO_2 deposition during the second PECVD process provides valuable insights into the optical characteristics of the heterostructures. Higher SiO_2 deposition temperatures, resulting in smaller FSR values, are indicative of a higher effective refractive index (n_{eff}^{gpe}) and an enhanced guiding mode. This is attributed to the heightened reactivity of oxygen at higher deposition temperature, resulting in an accelerated kinetic deposition and an increased thickness of the deposited element within a given time frame (1 minute). Considering the insights from the ellipsometric analysis in the previous section, a thicker Si/SiO_2 bi-layer decreases its effective index (close to $n_{bi\text{-}layer}$≈1.6 at 800 nm, Fig. 14.). As the bi-layer thickness is sub-micronic (< 100 nm) and its refractive index is higher than that of the air, this bi-layer raises the thickness of the core implying an increase in the effective refractive index. Indeed, in a four slab-layer structure, there is two distinct families of solutions for guided modes [75]. The first family involves optical mode confined inside the UV210 core and propagating in the cone of light defined by the wave vector relation $k_0.n_{bi\text{-}layer} \leq k_0.n_{eff} \leq k_0.n_{core}$, while the second family involves mode propagating in the cone of light defined by $k_0.n_{air} \leq k_0.n_{eff} \leq k_0.n_{core}$. Decreasing FSR measurements (increasing n_{eff}) with an increasing silica temperature deposition reveals the structure support a propagating mode of the type II family. At the beginning of the material growth, the bi-layer thickness increase the core thickness guiding layer. If the deposition process allows a thicker bi-layer, only then it role will switch as a superior cladding. Consequently, the structure will predominantly exhibit type I family modes, wherein the refractive index of the bi-layer ($n_{bi\text{-}layer}$) supplants that of the surrounding air (n_{air}). In integrated photonics the dispersion curve depicting the effective refractive index as a function of the guiding layer height consistently rises with an increase in the guiding layer height. In other words, this Si/SiO_2 bi-layer corresponds to a symmetrization of the structure. In this scenario and theory, there is a shift of the dispersion curve to thinner guided layer thickness, resulting in a decrease in the cut-off thickness. With higher temperature deposition, there is a thicker bi-layer (thus a thicker guided layer), leading to an increase in the effective refractive index of the structure, measurable by a decrease in the FSR. Notably, a linear increase in the temperature deposition of the SiO_2 results in a non-linear increase in the bi-layer thickness, inducing a non-linear increase in the effective refractive index or a non-linear decrease in the measured FSR (Tab. 9 and Fig. 17). The ability to provide continuous feedback on the dynamic change of the material by tracking the FSR evolution enables the incorporation of these chips for real-time monitoring of thickness evolution during material growth. It is noteworthy that such resonant structures arranged in PECVD reactors would serve as excellent probes for real-time

measurements of layer deposition parameters. Furthermore, a judicious adjustment of the bilayer and composition thickness enable a precise control of the FSR value which may be necessary for certain sensing applications.

	SiO_2 upper cladding deposition
$Si/SiO_2/UV210/Si_{amorphous}$	None
	SiO_2 : 1 min at 120°C
	SiO_2 : 1 min at 135°C
	SiO_2 : 1 min at 150°C

Tab. 8. PECVD temperature deposition for the SiO_2 upper cladding deposition.

SiO_2 temperature deposition	**FSR**	n_{eff}^{gpe}
120°C	8.183	1.865
135°C	7.980	1.912
150°C	7.316	2.086

Tab. 9. Average FSR and the associated n_{eff}^{gpe} for the three heterostructures with three various SiO_2 temperature deposition.

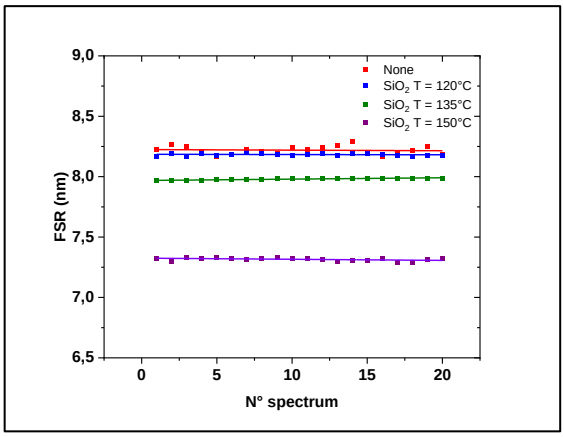

Fig. 17. Statistical measurements of the FSR for four types of heterostructures with various upper SiO_2 layer temperature deposition.

5. Conclusion

The comprehensive investigation of the fabrication, characterization, and optical evaluation of symmetrical heterostructures Si/SiO2/UV210/Si/SiO2 has provided valuable insights into their physical, chemical, and optical characteristics. The successful implementation of the photolithographic process onto the organic UV210, followed by low-temperature PECVD processes, enable the realization of symmetrical SOI with Org. Processes have successfully achieved the objective of protecting the organic UV210 layer from potential aggressive agents during sensing applications through the implementation of the Si/SiO_2 upper cladding. Meticulous characterizations on various heterostructures involving Raman spectroscopy, X-ray Photoelectron Spectroscopy (XPS), and ellipsometry have offered a comprehensive understanding of the composition of the deposited upper cladding above the organic layer. Optical measurements on different heterostructure, particularly the study of the Free Spectral Range (FSR), have highlighted the sensitivity of resonant structures to deposition conditions, providing nuanced control over their optical properties. A higher SiO_2 temperature deposition result in an increased guided layer thickness that contributes to the increase of the effective refractive index measured by the FSR tracking evolution. This underscores the potential for controlling material growth through the measurement of optical resonances plus a precise selection of the FSR value by adjusting the upper cladding properties. Furthermore, the incorporation of nano-particles within the organic UV210 layer encapsulated between two Si/SiO_2 bi-layer leads the way for generating light and frequency comb in nonlinear optics applications.

Acknowledgments

The authors thank the “Fondation d’Entreprise Grand Ouest” (BPGO) plus the Fondation Rennes of the University of Rennes for the financial support of this work. The authors also thank the NanoRennes platform for the DUV processes and ellipsometry measurement, the Scan Mat service unit for Raman analyses and the Promes-CNRS and CIRIMAT laboratories for XPS analyses.

Appendix A. Supplementary data

Supplementary data to this article can be found online at *“doi”.*

References

[1] X. Chen, C. Li, H.K. Tsang, Device engineering for silicon photonics, NPG Asia Mater 3 (2011) 34–40. https://doi.org/10.1038/asiamat.2010.194.

[2] S. Suzuki, K. Oda, Y. Hibino, Integrated-optic double-ring resonators with a wide free spectral range of 100 GHz, Journal of Lightwave Technology 13 (1995) 1766–1771. https://doi.org/10.1109/50.405322.

[3] P. Rabiei, W.H. Steier, C. Zhang, L.R. Dalton, Polymer micro-ring filters and modulators, Journal of Lightwave Technology 20 (2002) 1968–1975. https://doi.org/10.1109/JLT.2002.803058.

[4] X.-Y. Wang, C.-S. Ma, S.-L. E, X. Yan, Y.-Z. Xu, H.-M. Zhang, D.-M. Zhang, Z.-C. Cui, D.-G. Sun, Parameter optimization and characteristic analysis of a polymer microring resonant wavelength multiplexer, Optics & Laser Technology 37 (2005) 337–344. https://doi.org/10.1016/j.optlastec.2004.04.016.

[5] J.H. Schmid, P. Cheben, P.J. Bock, R. Halir, J. Lapointe, S. Janz, A. Delage, A. Densmore, J.-M. Fedeli, T.J. Hall, B. Lamontagne, R. Ma, I. Molina-Fernandez, D.-X. Xu, Refractive Index Engineering With Subwavelength Gratings in Silicon Microphotonic Waveguides, IEEE Photonics Journal 3 (2011) 597–607. https://doi.org/10.1109/JPHOT.2011.2139198.

[6] V.M.N. Passaro, C.D. Tullio, B. Troia, M.L. Notte, G. Giannoccaro, F.D. Leonardis, Recent Advances in Integrated Photonic Sensors, Sensors 12 (2012) 15558–15598. https://doi.org/10.3390/s121115558.

[7] N.L. Kazanskiy, S.N. Khonina, M.A. Butt, Advancement in Silicon Integrated Photonics Technologies for Sensing Applications in Near-Infrared and Mid-Infrared Region: A Review, Photonics 9 (2022) 331. https://doi.org/10.3390/photonics9050331.

[8] C. Delezoide, Polymer microring resonators for optofluidic evanescent field sensors, Ph.D thesis, University of Paris-Saclay / ENS, 2012.

[9] C. Delezoide, M. Salsac, J. Lautru, H. Leh, C. Nogues, J. Zyss, M. Buckle, I. Ledoux-Rak, C.T. Nguyen, Vertically Coupled Polymer Microracetrack Resonators for Label-Free Biochemical Sensors, IEEE Photon. Technol. Lett. 24 (2012) 270–272. https://doi.org/10.1109/LPT.2011.2177518.

[10] Chung-Yen Chao, W. Fung, L.J. Guo, Polymer microring resonators for biochemical sensing applications, IEEE J. Select. Topics Quantum Electron. 12 (2006) 134–142. https://doi.org/10.1109/JSTQE.2005.862945.

[11] H. Zhu, I.M. White, J.D. Suter, M. Zourob, X. Fan, Opto-fluidic micro-ring resonator for sensitive label-free viral detection, Analyst 133 (2008) 356. https://doi.org/10.1039/b716834a.

[12] A. Francois, M. Himmelhaus, Optical biosensor based on whispering gallery mode excitations in clusters of microparticles, Applied Physics Letters 92 (2008) 141107. https://doi.org/10.1063/1.2907491.

[13] A.-F. Obaton, Y. Sanogo, C. Yardin, J. Lautru, C. Lyathaud, J. Dubard, N. Fischer, Association of vertically coupled polymer micro-resonator and phase-sensitive optical low coherence interferometer for label-free biosensing applications, Metrologia 51 (2013) 1. https://doi.org/10.1088/0026-1394/51/1/1.

[14] L. Garnier, H. Lhermite, V. Vié, O. Pin, Q. Liddell, H. Cormerais, E. Gaviot, B. Bêche, Monitoring the evaporation of a sessile water droplet by means of integrated photonic resonator, J. Phys. D: Appl. Phys. 53 (2020) 125107. https://doi.org/10.1088/1361-6463/ab651d.

[15] R. Castro-Beltrán, L. Garnier, A. Saint-Jalmes, H. Lhermite, H. Cormerais, A.-L. Fameau, E. Gicquel, B. Bêche, Microphotonics for monitoring the supramolecular thermoresponsive behavior of fatty acid surfactant solutions, Optics Communications 468 (2020) 125773. https://doi.org/10.1016/j.optcom.2020.125773.

[16] L.A. Eldada, Polymer integrated optics: promise versus practicality, in: Organic Photonic Materials and Devices IV, SPIE, 2002: pp. 11–22. https://doi.org/10.1117/12.470454.

[17] I.C.C. de M. Porto, Polymer Biocompatibility, in: Polymerization, IntechOpen, 2012. https://doi.org/10.5772/47786.

[18] J. Scheuer, Fabrication and Characterization of low-loss polymeric waveguides and micro-resonators, in: Integrated Photonics and Nanophotonics Research and Applications / Slow and Fast Light (2007), Paper ITuA3, Optica Publishing Group, 2007: p. ITuA3. https://doi.org/10.1364/IPNRA.2007.ITuA3.

[19] A. Maalouf, M. Gadonna, D. Bosc, I. Hardy, Integrated polymers (PVCi/PMATRIFE) microring resonators for low power tunable filters, Optics Communications 285 (2012) 4088–4091. https://doi.org/10.1016/j.optcom.2012.05.043.

[20] B. Bêche, N. Pelletier, E. Gaviot, J. Zyss, Single-mode TE_{00} – TM_{00} optical waveguides on SU-8 polymer, Optics Communications 230 (2004) 91–94. https://doi.org/10.1016/j.optcom.2003.11.016.

[21] N. Pelletier, B. Beche, E. Gaviot, L. Camberlein, N. Grossard, F. Polet, J. Zyss, Single-mode rib optical waveguides on SOG/SU-8 polymer and integrated Mach-Zehnder for designing thermal sensors, IEEE Sensors J. 6 (2006) 565–570. https://doi.org/10.1109/JSEN.2006.874489.

[22] D. Duval, H. Lhermite, C. Godet, N. Huby, B. Bêche, Fabrication and optical characterization of sub-micronic waveguide structures on UV210 polymer, J. Opt. 12 (2010) 055501. https://doi.org/10.1088/2040-8978/12/5/055501.

[23] L. Garnier, J. Gastebois, H. Lhermite, V. Vié, A. Saint-Jalmes, H. Cormerais, E. Gaviot, B. Bêche, On the detection of nanoparticle cloud migration by a resonant photonic surface signal towards sedimentation velocity measurements, Results in Optics 12 (2023) 100430.

[24] J. Gastebois, H. Lhermite, H. Cormerais, A.S. Jalmes, V. Vié, L. Garnier, B. Bêche, An innovative optical viscometer using a resonant surface signal, in: Optical Methods for Inspection, Characterization, and Imaging of Biomaterials VI, SPIE, 2023: pp. 121–129. https://doi.org/10.1117/12.2672418.
[25] G. Gajdátsy, F. Benedek, J. Kokavecz, G. Szabó, J. Kornis, Improved fiber optic device for in situ determination of electrolyte stratification in lead-acid batteries, Review of Scientific Instruments 80 (2009) 125108. https://doi.org/10.1063/1.3272201.
[26] H. Guo, L. Wan, J. Tang, S. Wu, Z. Su, N. Sharma, Y. Fang, Z. Liu, C. Zhao, Stable colloid-in-acid electrolytes for long life proton batteries, Nano Energy 102 (2022) 107642. https://doi.org/10.1016/j.nanoen.2022.107642.
[27] L. Zhang, G. Yang, C. Yang, G. Que, Study on Colloidal Model of Petroleum Residues through the Attraction Potential between Colloids, International Journal of Analytical Chemistry 2016 (2016) e4182164. https://doi.org/10.1155/2016/4182164.
[28] H. Vasconcelos, A.B.M. Teixeira, J. Mendes, J. Araújo, B. Dias, P.A.S. Jorge, C.M. Saraiva, L.C.C. Coelho, J.M.M.M. de Almeida, Optical biosensor for the detection of low concentrations of hydrogen peroxide in milk samples, in: Optical Sensing and Detection VII, SPIE, 2022: pp. 252–257. https://doi.org/10.1117/12.2621552.
[29] L. Lanotte, F. Boissel, P. Schuck, R. Jeantet, C. Le Floch-Fouéré, Drying-induced mechanisms of skin formation in mixtures of high protein dairy powders, Colloids and Surfaces A: Physicochemical and Engineering Aspects 553 (2018) 20–27. https://doi.org/10.1016/j.colsurfa.2018.05.020.
[30] T. Tamir, ed., Guided-Wave Optoelectronics, Springer, Berlin, Heidelberg, 1988. https://doi.org/10.1007/978-3-642-97074-0.
[31] R.G. Hunsperger, Integrated Optics, Springer, New York, NY, 2009. https://doi.org/10.1007/b98730.
[32] A.J. Hussein, S.A. Taya, D. Vigneswaran, R. Udiayakumar, A. Upadhyay, T. Anwar, I.S. Amiri, Universal dispersion curves of a planar waveguide with an exponential graded-index guiding layer and a nonlinear cladding, Results in Physics 20 (2021) 103734. https://doi.org/10.1016/j.rinp.2020.103734.
[33] D. Rafizadeh, J.P. Zhang, S.C. Hagness, A. Taflove, K.A. Stair, S.T. Ho, R.C. Tiberio, Waveguide-coupled AlGaAs/GaAs microcavity ring and disk resonators with high finesse and 21.6-nm free spectral range, Opt. Lett., OL 22 (1997) 1244–1246. https://doi.org/10.1364/OL.22.001244.
[34] T. Indukuri, P. Koonath, B. Jalali, Subterranean silicon photonics: Demonstration of buried waveguide-coupled microresonators, Applied Physics Letters 87 (2005) 081114. https://doi.org/10.1063/1.2009062.
[35] E. Marchena, B. Redding, T. Creazzo, S. Shi, D.W. Prather, Whispering gallery modes at 800 nm and 1550 nm in concentric Si-nc/Er:SiO2 microdisks, JNP 4 (2010) 049501. https://doi.org/10.1117/1.3312634.
[36] A. Layadi, A. Vonsovici, R. Orobtchouk, D. Pascal, A. Koster, Low-loss optical waveguide on standard SOI/SIMOX substrate, Optics Communications 146 (1998) 31–33. https://doi.org/10.1016/S0030-4018(97)00600-7.
[37] F.C. Blom, H. Kelderman, H.J.W.M. Hoekstra, A. Driessen, Th.J.A. Popma, S.T. Chu, B.E. Little, A single channel dropping filter based on a cylindrical microresonator, Optics Communications 167 (1999) 77–82. https://doi.org/10.1016/S0030-4018(99)00296-5.
[38] L. Vivien, S. Laval, B. Dumont, S. Lardenois, A. Koster, E. Cassan, Polarization-independent single-mode rib waveguides on silicon-on-insulator for telecommunication wavelengths, Optics Communications 210 (2002) 43–49. https://doi.org/10.1016/S0030-4018(02)01681-4.
[39] W. Bogaerts, V. Wiaux, D. Taillaert, S. Beckx, B. Luyssaert, P. Bienstman, R. Baets, Fabrication of photonic crystals in silicon-on-insulator using 248-nm deep UV lithography, IEEE Journal of Selected Topics in Quantum Electronics 8 (2002) 928–934. https://doi.org/10.1109/JSTQE.2002.800845.
[40] A. Densmore, D.-X. Xu, P. Waldron, S. Janz, P. Cheben, J. Lapointe, A. Delage, B. Lamontagne, J.H. Schmid, E. Post, A Silicon-on-Insulator Photonic Wire Based Evanescent Field Sensor, IEEE Photonics Technology Letters 18 (2006) 2520–2522. https://doi.org/10.1109/LPT.2006.887374.
[41] C.A. Barrios, K.B. Gylfason, B. Sánchez, A. Griol, H. Sohlström, M. Holgado, R. Casquel, Slot-waveguide biochemical sensor, Opt. Lett., OL 32 (2007) 3080–3082. https://doi.org/10.1364/OL.32.003080.
[42] F. Khozeymeh, M. Razaghi, T. Chalyan, L. Pavesi, Fast analytical modelling of an SOI micro-ring resonator for bio-sensing application, J. Phys. D: Appl. Phys. 51 (2018) 285401. https://doi.org/10.1088/1361-6463/aac865.
[43] UV™ 210GS Positive DUV Photoresist | Kayaku Advanced Materials, (n.d.). https://kayakuam.com/products/uv-210gs-positive-duv-photoresist/.
[44] P.B. Sahoo, R. Vyas, M. Wadhwa, S. Verma, Progress in deep-UV photoresists, Bull Mater Sci 25 (2002) 553–556. https://doi.org/10.1007/BF02710549.
[45] M.F. Ceiler, P.A. Kohl, S.A. Bidstrup, Plasma-Enhanced Chemical Vapor Deposition of Silicon Dioxide Deposited at Low Temperatures, J. Electrochem. Soc. 142 (1995) 2067. https://doi.org/10.1149/1.2044242.
[46] Plateforme nR (nanoRennes) | Institut d'Electronique et des Technologies du numéRique, (n.d.). https://www.ietr.fr/plateforme-nr-nanorennes (accessed November 20, 2023).
[47] Q. Li, V. Vié, H. Lhermite, E. Gaviot, C. Bourlieu, A. Moréac, D. Morineau, D. Dupont, S. Beaufils, B. Bêche, Polymer resonators sensors for detection of sphingolipid gel/fluid phase transition and melting temperature measurement, Sensors and Actuators A: Physical 263 (2017) 707–717. https://doi.org/10.1016/j.sna.2017.07.037.

[48] N. Colthup, Introduction to Infrared and Raman Spectroscopy, Elsevier, 2012.
[49] K. Kandoussi, C. Simon, N. Coulon, T. Mohammed-Brahim, A. Moreac, Undoped and arsenic-doped low temperature (∼165°C) microcrystalline silicon for electronic devices process, Journal of Non-Crystalline Solids 352 (2006) 968–971. https://doi.org/10.1016/j.jnoncrysol.2005.11.147.
[50] F.L. Galeener, G. Lucovsky, Longitudinal Optical Vibrations in Glasses: GeO_2 and SiO_2, Phys. Rev. Lett. 37 (1976) 1474–1478. https://doi.org/10.1103/PhysRevLett.37.1474.
[51] G. Lucovsky, F.L. Galeener, Intermediate range order in amorphous solids, Journal of Non-Crystalline Solids 35–36 (1980) 1209–1214. https://doi.org/10.1016/0022-3093(80)90362-2.
[52] F.L. Galeener, J.C. Mikkelsen, Raman studies of the thermal oxide of silicon, Solid State Communications 37 (1981) 719–723. https://doi.org/10.1016/0038-1098(81)91085-1.
[53] D. Briggs, M.P. Seah, Practical Surface Analysis, Auger and X-ray Photoelectron Spectroscopy, Wiley, 1990.
[54] D.A. Shirley, High-Resolution X-Ray Photoemission Spectrum of the Valence Bands of Gold, Phys. Rev. B 5 (1972) 4709–4714. https://doi.org/10.1103/PhysRevB.5.4709.
[55] R. Berjoan, E. Beche, J.A. Roger, C.H.S. Dupuy, XPS and AES analysis of SiO thin film. A comparative study with Si, SiO2, and a Si/SiO2 interlayer, in: Journal of high temperature chemical processes, 1994: pp. 555–565. http://pascal-francis.inist.fr/vibad/index.php?action=getRecordDetail&idt=3516498 (accessed April 4, 2024).
[56] H. Hantsche, High resolution XPS of organic polymers, the scienta ESCA300 database. By G. Beamson and D. Briggs, Wiley, Chichester 1992, 295 pp., hardcover, £ 65.00, ISBN 0-471-93592-1, Advanced Materials 5 (1993) 778–778. https://doi.org/10.1002/adma.19930051035.
[57] J.F. Moulder, J. Chastain, eds., Handbook of X-ray photoelectron spectroscopy: a reference book of standard spectra for identification and interpretation of XPS data, Update, Perkin-Elmer Corporation, Eden Prairie, Minn, 1992.
[58] Justin Gorham, NIST X-ray Photoelectron Spectroscopy Database - SRD 20, (2012). https://doi.org/10.18434/T4T88K.
[59] H.R. Philipp, Optical and bonding model for non-crystalline SiOx and SiOxNy materials, Journal of Non-Crystalline Solids 8–10 (1972) 627–632. https://doi.org/10.1016/0022-3093(72)90202-5.
[60] R. Alfonsetti, L. Lozzi, M. Passacantando, P. Picozzi, S. Santucci, XPS studies on SiOx thin films, Applied Surface Science 70–71 (1993) 222–225. https://doi.org/10.1016/0169-4332(93)90431-A.
[61] J. Viard, E. Beche, J. Durand, R. Berjoan, SiH bonding environment in PECVD a-SiOxNy:H thin films, Journal of the European Ceramic Society 17 (1997) 2029–2032. https://doi.org/10.1016/S0955-2219(97)00083-6.
[62] M.P. Seah, S.J. Spencer, Ultrathin SiO2 on Si IV. Intensity measurement in XPS and deduced thickness linearity, Surface and Interface Analysis 35 (2003) 515–524. https://doi.org/10.1002/sia.1565.
[63] Yu.N. Novikov, V.A. Gritsenko, Short-range order in amorphous SiOx by x ray photoelectron spectroscopy, Journal of Applied Physics 110 (2011) 014107. https://doi.org/10.1063/1.3606422.
[64] S. Ohno, K. Inoue, M. Morimoto, S. Arae, H. Toyoshima, A. Yoshigoe, Y. Teraoka, S. Ogata, T. Yasuda, M. Tanaka, Time-evolution of thermal oxidation on high-index silicon surfaces: Real-time photoemission spectroscopic study with synchrotron radiation, Surface Science 606 (2012) 1685–1692. https://doi.org/10.1016/j.susc.2012.07.011.
[65] A.A. Gismatulin, V.A. Voronkovskii, G.N. Kamaev, Y.N. Novikov, V.N. Kruchinin, G.K. Krivyakin, V.A. Gritsenko, I.P. Prosvirin, A. Chin, Electronic structure and charge transport mechanism in a forming-free SiOx-based memristor, Nanotechnology 31 (2020) 505704. https://doi.org/10.1088/1361-6528/abb505.
[66] D. Briggs, M.P. Seah, Practical Surface Analysis, Auger and X-ray Photoelectron Spectroscopy, Wiley, 1990.
[67] T.R. Gengenbach, G.H. Major, M.R. Linford, C.D. Easton, Practical guides for x-ray photoelectron spectroscopy (XPS): Interpreting the carbon 1s spectrum, Journal of Vacuum Science & Technology A 39 (2021) 013204. https://doi.org/10.1116/6.0000682.
[68] V. Serin, E. Beche, R. Berjoan, D. Dorignac, D. Rats, J. Fontaine, L. Vandenbulcke, C. Germain, A. Catherinot, XAES, XPS, EELS and Raman spectroscopy of polycrystalline to amorphous films with various sp2 to sp3 bondings, in: 1998.
[69] D. Ballutaud, N. Simon, H. Girard, E. Rzepka, B. Bouchet-Fabre, Photoelectron spectroscopy of hydrogen at the polycrystalline diamond surface, Diamond and Related Materials 15 (2006) 716–719. https://doi.org/10.1016/j.diamond.2006.01.004.
[70] M. Giesbers, A.T.M. Marcelis, H. Zuilhof, Simulation of XPS C1s Spectra of Organic Monolayers by Quantum Chemical Methods, Langmuir 29 (2013) 4782–4788. https://doi.org/10.1021/la400445s.
[71] T. Duguet, C. Bessaguet, M. Aufray, J. Esvan, C. Charvillat, C. Vahlas, C. Lacaze-Dufaure, Toward a computational and experimental model of a poly-epoxy surface, Applied Surface Science 324 (2015) 605–611. https://doi.org/10.1016/j.apsusc.2014.10.096.
[72] H. Fujiwara, Spectroscopic Ellipsometry: Principles and Applications, John Wiley & Sons, 2007.
[73] T. Begou, B. Bêche, A. Goullet, J.-P. Landesman, A. Granier, C. Cardinaud, E. Gaviot, L. Camberlein, N. Grossard, G. Jézéquel, J. Zyss, First developments for photonics integrated on plasma-polymer-HMDSO: Single-mode TE_{00}-TM_{00} straight waveguides, Optical Materials 30 (2007) 657–661. https://doi.org/10.1016/j.optmat.2007.02.049.
[74] G.E. Jellison, V.I. Merkulov, A.A. Puretzky, D.B. Geohegan, G. Eres, D.H. Lowndes, J.B. Caughman, Characterization of thin-film amorphous semiconductors using spectroscopic ellipsometry, Thin Solid Films 377–378 (2000) 68–73. https://doi.org/10.1016/S0040-6090(00)01384-5.

[75] B. Bêche, E. Gaviot, A. Renault, J. Zyss, F. Artzner, Another way to shape the comprehensive analytical approach describing electromagnetic energy distribution through four-slab-layer structures, Optik 121 (2010) 188–194. https://doi.org/10.1016/j.ijleo.2008.06.006.